Coupling a weather model directly to GNSS orbit determination - case studies with OpenIFS

Angel Navarro Trastoy[1], Sebastian Strasser[2], Lauri Tuppi[1], Maksym Vasiuta[1], Markku Poutanen[3], Torsten Mayer-Gürr[2], and Heikki Järvinen[1]

[1]Institute for Atmospheric and Earth System Research / Physics, Faculty of Science, University of Helsinki, Finland
[2]Institute of Geodesy, Graz University of Technology, Austria
[3]Finnish Geospatial Research Institute, National Land Survey of Finland

Correspondence: Heikki Järvinen (heikki.j.jarvinen@helsinki.fi)

Abstract.

Neutral gas atmosphere bends and delays propagation of microwave signals in satellite-based navigation. Weather prediction models can be used to estimate these effects by providing 3-dimensional refraction fields to ray-trace the signal delays. In this study, a global numerical weather prediction model (Open Integrated Forecasting System (OpenIFS) licensed for Academic use by the European Centre for Medium-Range Weather Forecast) is used to generate the refraction fields. The ray-traced slant delays are supplied as such – in contrast to mapping – for an orbit solver (GROOPS (Gravity Recovery Object Oriented Programming System) software toolkit of Graz University of Technology) which applies the raw observation method. Here we show that such a close coupling is possible without need for major additional modifications in the solver codes. The main finding here is that the adopted approach provides a very good *a priori* model for the atmospheric effects on navigation signals. We suspect that removal of the intermediate mapping step allows to take advantage of the local refraction field asymmetries in the GNSS signal processing. Moreover, the direct coupling helps in identifying deficiencies in the slant delay computation because the modelling errors are not convoluted in the mapping procedures. These conclusions appear robust, despite the relatively small data set of raw code and phase observations covering the core network of 66 ground-based stations of the International GNSS Service over one-month periods in December 2016 and June 2017. More generally, the new configuration enhances our control of geodetic and meteorological aspects of the orbit problem. This is pleasant because we can, for instance, regulate at will the weather model output frequency and increase coverage of spatio-temporal aspects of weather variations. The direct coupling of a weather model in precise GNSS orbit determination presented in this paper provides a unique framework for benefiting even more widely than previously the apparent synergies in space geodesy and meteorology.

1 Introduction

Refraction in the neutral gas atmosphere bend and delay global navigation system satellite (GNSS) signals (Bevis et al., 1992). These atmospheric effects cannot be deduced based on GNSS measurements alone because the signal propagation is identical for all frequencies typically applied in GNSS. Some auxiliary information is therefore needed to correct these tropospheric effects (Guerova et al., 2016). Global numerical weather prediction (NWP) systems are currently the best source

of such support since they ingest tens of millions of observations every day from global meteorological observing systems and constantly update the atmospheric state with the latest data (Bauer et al., 2015).

State-of-the-art in correcting the tropospheric effects in precise orbit determination (POD) of GNSS is based on the use of mapping functions (e.g., Böhm et al., 2006; Niell, 1996; Rocken et al., 2001; Zus et al., 2014). These are designed to encapsulate essential atmospheric effects by a small number of parameters. The functional form of the Vienna mapping function (VMF3; Landskron and Böhm, 2018), for instance, represents the tropospheric delay effect with three mapping coefficients, and has a dependency to the elevation angle but not to the azimuthal angle. This concise representation makes mapping functions generally easy to apply and exchange but also truncates atmospheric information contained in weather models. In particular, they are not designed to represent azimuthal asymmetries which can be significant, depending on the site and weather of the day (Eresmaa et al., 2007, 2008a).

This article presents a new configuration where a NWP model is directly coupled with a GNSS orbit solver, thus effectively omitting the use of mapping functions. Our aim is to study the impact of loss-less use of weather model data in orbit determination. To this end, we have first analyzed the performance of the tropospheric delays produced by both systems (VMF3 and OpenIFS), providing the so called 'a priori' models. Then we have analyzed the differences of these two models in a real case, by correcting the *a priori* model by fitting parameters in a least squares process. To our knowledge, this has not been attempted before on global scale but there are some useful early precedents. Nordman et al. (2007, 2009) applied directly the tropospheric slant-path corrections derived from a limited area weather model to a regional network solution of the Global Positioning System (GPS) receivers and reported a neutral-to-positive impact. A fairly similar approach was adopted in Hobiger et al. (2008) who concentrated on precise point positioning in a regional GPS network. Finally, Eriksson et al. (2014) applied tropospheric corrections directly and noticed a sizable improvement in a very long baseline interferometry (VLBI) application by omitting the mapping step. Promisingly, Zus et al. (2014) concluded that computational performance of the best codes to compute tropospheric slant-path corrections is no longer a limiting factor in GNSS processing to side-line the mapping step.speed up

In this study, we have used OpenIFS at an affordable resolution (T$_L$639L91, see section 2.2) and a version of the least traveltime (LTT) ray-tracer used in Eresmaa et al. (2008b). We acknowledge that this setup does not utilize the full potential of production of slant-path corrections yet. Firstly, the LTT ray-tracer does not fully follow Rodgers (2000) (see section 2.3), and secondly, the resolution of OpenIFS can be increased further. However, even though a study and improvement of the ray-tracer could be done, it is out of the scope of this paper and will be addressed in an upcoming publication, as this setup allows us to experiment with the new configuration. This article is organized as follows. Data and methods are presented in Section 2, results in Section 3 followed by a discussion in Section 4 and the conclusions in section 5.

2 Data and methods

This section explains the data and methods applied in the new configuration to solve the GNSS orbit problem. It should be noted that all input data and different solver codes reside in the same super-computer, that is CSC – the IT Center for Science in Finland (for system specifications, please see CSC, 2021). Different work flow components (running the weather model,

production of the slant delay data, and solving the GNSS orbits) are interlaced but managed as separate tasks. Also, all these components are assembled together as such with no lengthy fine tuning undertaken for obtaining the highest possible performance – neither in terms of computational optimization nor solution accuracy. This constitutes in other words a benchmark system where to build-on further improvements.

2.1 Precise orbit determination

The orbit determination process applied in this study is based on the raw observation approach (Schönemann et al., 2011; Schönemann, 2014) and follows the strategy detailed in Strasser et al. (2019). Raw code and phase observations from a network of 66 well-distributed ground-based stations of the International GNSS Service (IGS; Johnston et al., 2017) to the GPS satellite constellation are utilized to determine a set of geodetic parameters in an iterative least-squares adjustment. These observations are processed in daily batches at a 30-second sampling period (a total of 2880 observation epochs per day) using GROOPS (Mayer-Gürr et al., 2020), which is an open-source software package for GNSS processing and gravity field determination developed at Graz University of Technology. The observations are connected to the parameters via the code and phase observation equations (e.g., Hauschild, 2017), which encompass corrections for various effects, one of which is the tropospheric influence.

The geometry is contained in the observation equations as the range between satellite and station positions. Satellite orbits are numerically integrated over 24 hours based on force models, such as Earth's gravity field, tidal forces, and radiation pressure (cf. Strasser et al., 2019, for a complete list). These dynamic orbits are then fitted to the observations in the least-squares adjustment by estimating their initial position and velocity as well as a set of solar radiation pressure parameters (Arnold et al., 2015), as this force cannot be modeled adequately in advance. In addition, small instantaneous velocity changes, pseudo-stochastic pulses (e.g., Hugentobler and Montenbruck, 2017), are estimated at the center of each 24-hour orbit arc to consider orbit modeling deficiencies. These are not based on physical models but corrections to deficiencies in the calculations.

Next to the orbit parameters, various other parameters are estimated in the least-squares adjustment. These comprise static station positions, Earth orientation parameters, epoch-wise clock errors and constant signal biases at each receiver and satellite, the ionospheric slant total electron content (STEC) per group of observations between a receiver and satellite at one epoch, and phase ambiguities. The ambiguities are resolved to integer values during processing.

Following Petit and Luzum (2010), the tropospheric slant delay for a line-of-sight observation between a satellite and receiver is

$$T_{SD} = m_h(e)D_{zh} + m_w(e)D_{zw} + m_g(e)[G_N \cos a + G_E \sin a]. \tag{1}$$

Here, e and a are the elevation and azimuth angles at the receiver antenna, D_{zh} is the zenith hydrostatic delay, D_{zw} is the zenith wet delay, and G_N and G_E are the horizontal delay gradients in north-south and east-west directions (the delays are expressed in meters). The mapping functions (m_h, m_w, and m_g) map the delays from zenith to the line-of-sight elevation. The

zenith delay mapping function is

$$m_{h,w}(e) = \frac{1 + \dfrac{a}{1 + \dfrac{b}{1 + c}}}{\sin e + \dfrac{a}{\sin e + \dfrac{b}{\sin e + c}}}, \tag{2}$$

where a, b, and c are mapping coefficients (Herring, 1992; Niell, 1996). The gradient mapping function is

$$m_g(e) = \frac{1}{\sin e \tan e + C} \tag{3}$$

with $C = 0.0031$ for the hydrostatic effect and $C = 0.0007$ for the wet effect (Chen and Herring, 1997).

In the default system, *a priori* tropospheric corrections are based on VMF3 operational data (Landskron and Böhm, 2018). The model provides zenith hydrostatic, zenith wet, hydrostatic gradient, and wet gradient delays as well as corresponding mapping function coefficients (a, b, c) on a global 1x1° grid at a 6-hour sampling period. Values for a specific station location and point in time are bilinearly interpolated from the surrounding grid points in the space domain and linearly interpolated in time. A height correction from orographic height to station height is applied as well (cf. Strasser et al., 2019).

In the experiment, on the other hand, OpenIFS-based slant delay sky-views (see Section 2.3) are used to determine *a priori* tropospheric delays. These sky-views comprise slant delays at a regular 1x1° azimuth-elevation grid ray-traced directly at the station coordinates with an hourly sampling period. The slant delay for a specific observation is then computed by interpolating the gridded slant delays to the azimuth and elevation of the observation and linearly interpolating in time between the hourly delay values. The interpolation in space domain is done linearly in azimuth direction and using a degree-5 polynomial in elevation direction to properly cover the rapid delay changes at low elevations. Since these slant delays are based directly on a weather model, they include all hydrostatic, wet, and gradient effects and no mapping functions need to be used.

For individual measurements, there is a discrepancy ΔT_{SD} between the *a priori* tropospheric slant delay and the actual delay affecting the measurement since the models are imperfect. If we assume that ΔT_{SD} is solely due to troposphere, we can write the tropospheric slant delay discrepancy by using Eq. 1 as

$$\Delta T_r^s = m_h(e)\Delta D_{zh} + m_w(e)\Delta D_{zw} + m_g(e)[\Delta G_N \cos a + \Delta G_E \sin a]. \tag{4}$$

Assuming that the hydrostatic delay is well modelled ($\Delta D_{zh} = 0$), the residual zenith wet (ΔD_{zw}) and gradient ($\Delta G_N, \Delta G_E$) delay parameters can be set up to consider the discrepancy between modeled and measured tropospheric influence. These station-wise parameters are set up or omitted in this study depending on the analysis. If included, ΔD_{zw} is parameterized as a degree-1 spline with 2-hourly nodes, while ΔG_N and ΔG_E are parameterized linearly over the 24 hours. The mapping functions required for this parametrization are determined using the VMF3 mapping coefficients. The same parametrization is used both in case of VMF3-based or OpenIFS-based *a priori* slant delays since the parametrization is independent of the *a priori* model.

2.2 Weather model

OpenIFS is a portable version of the Integrated Forecasting System (IFS) of the European Centre for Medium-Range Weather Forecasts (ECMWF). Essentially, it is a global weather prediction model with identical forecast skill as in the full IFS. Data assimilation is not explicitly included in OpenIFS, but it is included implicitly because external initial conditions of the atmospheric state (temperature, wind, humidity, and surface pressure) are applied. In this study, we use operational atmospheric analyses of ECMWF (Ollinaho et al., 2021) and OpenIFS version 43r3v1 that was part of the operational forecasting system at ECMWF from July 2017 to June 2018 (IFS cycle 43r3; ECMWF, 2019).

We simulate time evolution of the atmospheric state with OpenIFS at horizontal resolution T_L639, which corresponds to about 31 km grid spacing at the equator, and at 91 vertical levels. The model top is at 0.01 hPa, which is approximately at the altitude of 80 km. The model domain thus covers the entire neutral atmosphere of the Earth. The model time step is 15 minutes and the atmospheric state is output once every hour. For comparison, the ECMWF operational system at the time used 8 km grid spacing at 137 levels (ECMWF, 2019).

Atmospheric states for the hourly refraction computation for the months of December 2016 and June 2017 are formed as follows. A sequence of 12-hour forecasts is generated from the 00 and 12 UTC analyses. Thus, an analysis at 00 UTC and forecasts at 01, 02, ..., 11 UTC, and correspondingly, an analysis at 12 UTC and forecasts at 13, 14, ..., 23 UTC provide the hourly coverage for one 24-hour period. OpenIFS thus effectively extrapolates the atmospheric analyses to the full hours between the twice-a-day analysis times.

2.3 Slant delays

The tropospheric slant delays are computed with ray tracing based on a least traveltime (LTT) operator (Eresmaa et al., 2008b). LTT operates on a 2-dimensional plane defined by the satellite and receiver positions and the centre of the Earth. A 2-dimensional refractivity field is obtained by converting the 3-dimensional OpenIFS fields of atmospheric dry mass and moisture content to refractivity and interpolating to a desired 2-dimensional plane. Interpolation is bi-linear in horizontal and assumes exponential refractivity profile in vertical between the model levels.

The LTT algorithm performs ray tracing to construct the path, expressed in polar coordinates, which satisfies the following system of differential equations:

$$\frac{dr}{ds} = \cos\theta \tag{5a}$$

$$\frac{d\psi}{ds} = \frac{\sin\theta}{r} \tag{5b}$$

$$\frac{d\theta}{ds} = -\sin\theta \left[\frac{1}{r} + \left(\frac{\partial n}{\partial r} \right)_\psi \right] \tag{5c}$$

Here ds is a path element, r is distance from the Earth's centre, ψ is the counterpart for polar coordinates, θ is the zenith angle, and n the refractive index. Equations 5 are integrated with the fourth-order Runge-Kutta method starting from the receiver position ($r_{rec} = R_\oplus + h_{rec}$; $\psi_{rec} = 0$) in the initial direction stated as the geometrical zenith angle of the satellite

($\theta_{rec} = \theta_{geom}$). The integration ends when the satellite altitude is reached ($r_{end} = r_{sat}$). The integration yields a set of points ($r; \psi$) which satisfy these equations.

The total delay on a slanted path results from slowing down of the signal due to refractive index $n > 1$ and increasing signal path length due to signal bending. The path bending is due to the second term in Eq. 5c. Since geometrical zenith angle is used as the initial direction, an angular separation appears between the end point of the ray and the satellite location, i.e., $r_{end} = r_{sat}$ but $\psi_{end} \neq \psi_{sat}$. Therefore the calculation of the path and slant delay is repeated by using an updated θ'_{rec} as follows:

$$\theta'_{rec} = \theta_{geom} - (\psi_{end} - \psi_{sat}) = \theta_{geom} - \Delta\psi \tag{6}$$

In our implementation (Eresmaa et al., 2008b), the final slant delay is a linear combination of these two LTT calculations. This yields an angular difference of the order of $\Delta\psi \approx 10^{-4}$ rad for zenith angle $\theta = 85°$ and $\Delta\psi \approx 10^{-7}$ rad for $\theta = 10°$. Additional accuracy of the starting zenith angle could be obtained with additional iterations. This implementation does not completely follow Rodgers (2000) and therefore the results are sub-optimal. Efforts are ongoing to improve the LTT implementation, but this is out of the scope of this paper and it will be addressed in a future publication.

The effect of Earth flattening was evaluated for the slant delay computation since the LTT algorithm accounts for the Earth oblateness applying the concept of Euler radius. The magnitude of this effect was evaluated by degrading the Earth ellipsoid to a sphere thus changing the 2-dimensional plane projection onto the Earth surface. The effect was found to vary from -0.5 cm to $+1.5$ cm depending on the receiver latitude and antenna azimuth angle.

Here the LTT solver is applied such that instead of computing ray paths exactly in direction of the GNSS satellites in view, so-called sky-views are generated. They are constructed so that slant delays are calculated for zenith angles from 1 to 89 degrees and azimuth angles from 0 to 359 degrees with one degree increments in both directions, added with one calculation for the zenith delay. The sky-views are computed using the OpenIFS data at every full hour in December 2016 and June 2017 for the 66 selected IGS stations constituting the core network.

2.4 Performance metrics

In order to compare the experiments with the default system, the following performance metrics are defined. First, GNSS satellite orbits are determined for 24-hour periods. These 24-hour orbit arcs overlap at midnight (i.e., 00 UTC) between consecutive days, providing two independent positions **r** (expressed in meters) at a single epoch for each satellite. The differences between these positions are called orbit midnight discontinuities, as they represent jumps between two smooth orbit arcs. The discontinuity $\delta\mathbf{r}$ in the orbit position between consecutive days has components along (δr_a) and cross (δr_c) the orbit direction and a radial (δr_r) component in the local vertical. Running GROOPS using only *a priori* models (i.e., not estimating any corrections through fitted parameters according to Eq. 4) and analyzing the discontinuities we can compare the goodness of the models – the smaller the discontinuities are, the better is the *a priori* modelling. The associated performance metric $\|\delta\mathbf{r}\|$ is defined as:

$$\|\delta\mathbf{r}\| = \sqrt{(\delta r_a)^2 + (\delta r_c)^2 + (\delta r_r)^2} \tag{7}$$

for each satellite at each day boundary.

Second, as a part of the orbit determination, the *a priori* model for the troposphere can be corrected by fitting parameters in the least squares process (Eq. 4), producing the so-called *a posteriori* model. The fitted residual zenith wet delay (ΔD_{zw}) and gradient delays (ΔG_N and ΔG_E) are indicative of the goodness of the *a priori* model used – the smaller the corrections are, the better is the accuracy of the *a priori* model.

3 Results

The following results are aimed to demonstrate how the newly assembled experimental configuration (OpenIFS) performs in relation to a well-established default system (VMF3). According to the performance metrics explained in section 2.4, an analysis over the midnight discontinuities has been carried out, along with a study of the fitted parameters for the month of December 2016. To add statistical confidence to the results, we have also evaluated the month of June 2017 (Appendix A). The results are hoped to be indicative of the strengths and weaknesses of the experimental configuration, thus pointing to potential areas of further development.

3.1 Orbit midnight discontinuities

The orbit midnight discontinuities are a good metric to analyze how any factor, for instance tropospheric modelling, affects the quality of GNSS products. Figure 1a shows a color map where each cell represents the difference in the midnight discontinuity between the *a priori* default and experiment systems for a satellite over two consecutive days, as measured with $\|\delta\mathbf{r}\|$ (see eq. 7) and expressed in units of cm. Here, blue (red) means that discontinuities in the experimental system are smaller (larger) than in the default system.

(a) (b)
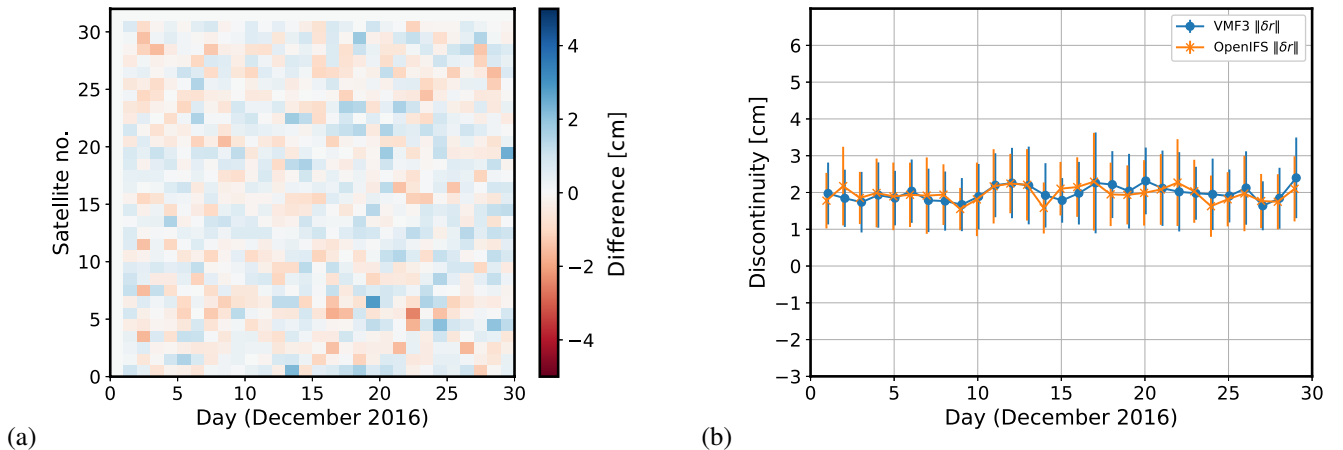
Figure 1. Norm of the midnight discontinuity ($\|\delta\mathbf{r}\|$) for December 2016. (a) A color map representing the difference between the default and experimental system for the satellites used in the experiment; (b) The mean (solid lines) and standard deviation (vertical whiskers) over all satellites for each day of the experiment with blue (default system) and orange (experimental system).

The differences in Fig. 1a are generally very small, of the order of a few cm. The mean covering all satellites over the whole period is 0.025 cm, pointing to slightly smaller discontinuities in the experimental system, although statistically negligible.

Next is shown a time-series of the mean values of the norm $\|\delta\mathbf{r}\|$ for all satellites (Fig. 1b), where the default system is in blue and the experiment in orange. Again, the results indicate that the experimental system has slightly smaller discontinuities. The mean values for the entire month are 1.961 cm for the experimental system and 1.986 cm for the default system. This difference, albeit small, is a rather systematic feature in Fig. 1b. Standard deviation around the mean value is 0.903 cm in the experimental system and 0.907 cm in the default system, showing a similar behaviour for both systems. The results presented in this section have been calculated not using Satellite G04 data due to malfunctions in the satellite or satellite-specific processing issues which are unrelated to tropospheric modelling, that were deteriorating the results for both systems used in the experiment.

3.2 Fitted tropospheric parameters

Next, the magnitude of the fitted parameters (ΔD_{zw}, ΔG_N and ΔG_E) is analyzed. Figure 2a shows the residual zenith wet delay (ΔD_{zw}) for both systems (default in blue, experiment in orange) over the month of December 2016. Each day is represented by the mean and standard deviation of all estimated values for all the stations used.

(a)   (b)
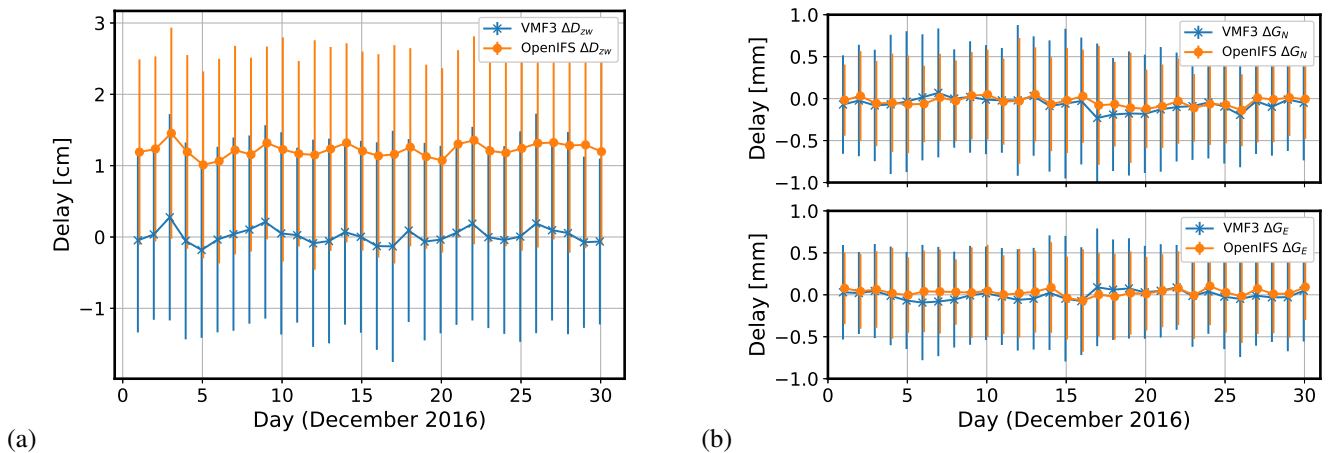
Figure 2. The mean and standard deviation of the fitted parameters: (a) zenith wet delay (ΔD_{zw}) and (b) North and East gradient delays (ΔG_N on top and ΔG_E at the bottom) for the a priori models for December 2016. Notation is as in Fig. 1

The mean fitted zenith wet delay (Figure 2a) is 1.220 cm in the experimental system and 0.016 cm in the default system. This is indicative of a severe and consistent positive bias in the experimental system while it is negligible for the default system. The positive bias can be interpreted such that in the experimental system the total slant delay is too small (i.e., the increased zenith wet delay compensates this deficiency in the least squares process). The possible reasons for the bias are further discussed in Section 4.

The standard deviation of fitted zenith wet delay values (Figure 2a) is $1.391 \, \mathrm{cm}$ in the experimental system and $1.349 \, \mathrm{cm}$ in the default system over the whole month. This is indicative of somewhat similar consistency of the default and experimental systems - despite the apparent bias, the variation of the fitted zenith wet delay values is similar to the default system.

The fitted gradient delays in the North and East directions are presented in Fig. 2b. The mean values over the month of December 2016 for ΔG_N and ΔG_E are very similar in both systems, $-0.035 \, \mathrm{mm}$ and $0.028 \, \mathrm{mm}$ for the experiment, and $-0.067 \, \mathrm{mm}$ and $-0.003 \, \mathrm{mm}$ for the default system. The standard deviations around these mean values are somewhat smaller in the experimental system, $0.527 \, \mathrm{mm}$ and $0.489 \, \mathrm{mm}$ for the experiment, and $0.706 \, \mathrm{mm}$ and $0.602 \, \mathrm{mm}$ for the default system, suggesting a marginal advantage over the default system.

3.3 Statistical significance of the experimental results

In order to add confidence on the results presented here, the experiment was repeated for the month of June 2017. This period covers a different phase of the Earth on its orbit around the sun, and thus generally different circumstances for the orbit problem. The central results are presented in Appendix A, and can be summarized as being very similar compared to the main study period. The conclusion is thus that the main study period of December 2016 seems to be representative for this type of studies.

4 Discussion

The default system of this study applies VMF3 delays and mapping function coefficients, which are computed from the ECMWF weather forecasts. The operational model version in December 2016 was very high-resolution, about $8 \, \mathrm{km}$ grid spacing at 137 model levels. The disseminated forecast fields for VMF3 computation are however interpolated from the full model resolution to one by one degree horizontal resolution at 25 standard pressure levels, which are available at six-hourly intervals. Lastly, VMF3 coefficients can be interpreted as a low-order representation of the tropospheric delay which does not represent, by design, azimuthal asymmetries in a receiver station sky-view. Despite these processing features, which all imply some loss of atmospheric information, VMF3 has proven to provide a hard-to-beat benchmark also in this study.

The experimental system applies a lower-resolution OpenIFS model version with about $31 \, \mathrm{km}$ grid spacing at 91 levels, which rather closely corresponds to the system applied in ensemble prediction at ECMWF. In this respect, the default system has a clear advantage in terms of simulation accuracy of atmospheric dynamics and physical processes. On the other hand, the subsequent processing in the experimental system is almost loss-less. We do interpolate the total tropospheric delay from a one by one degree sky-view to azimuth and elevation angles of an individual measurement, and interpolate in time from one-hourly model output fields to the measurement time. Other than that, the native OpenIFS refraction field is represented as such through the ray tracing step to the orbit solver. Technically, the ray tracing could be solved separately and directly corresponding to the azimuth and elevation angles of each measurement – in this case, time interpolation should also be omitted by gathering the measurements into time-slots closest to the model output time. Note that the OpenIFS model time step is 15 minutes in the experimental system and atmospheric fields could be output at the same frequency to reduce time interpolation effects.

245   Figure 2a is indicative of a sizable bias in the tropospheric *a priori* correction based on OpenIFS, where ΔD_{zw} is at the level of 0.73 cm throughout the period. This result prompted us to investigate more closely the total delay mean differences between VMF3 and OpenIFS. Indeed, at very low elevation angles the total delay in the experimental system differs systematically from the default system. This is very likely due to an approximation made in the LTT code regarding the geometrical effect on the signal path where the term $\frac{\cos\theta}{nr}(\frac{\partial n}{\partial \psi})_r$ in Eq. 5c is missing. Therefore, the LTT ray tracer applied in the experimental system

250 does not fully follow Rodgers (2000) and is sub-optimal. Work is ongoing to update the code. Importantly, the experimental system provides us with a solid reference where the weather model-based data is directly interfaced with GNSS measurements and orbit solutions with no intermediate and possibly obscuring processing steps. Thanks to this property, it led us to detect the problem with the implemented ray tracing code.

     The following question remains. Figure 2 tends to suggest that the tropospheric *a priori* model in the experimental system is

255 biased. How is it then possible that midnight discontinuities (Fig. 1) are comparable or even slightly smaller in the experimental system compared to the default system? A possible explanation is that the azimuthal asymmetries of the tropospheric delay that are present in the experimental system but are missing from the default system do matter and contribute to the orbit solutions. Essentially, the asymmetries are not systematic but they can systematically impact the system performance and the metrics presented here.

260   Finally, we have to keep in mind that only a small network of 66 stations are included in this study over a limited time period. A more comprehensive experiment will be prepared later including better GNSS station coverage and enhanced tropospheric modelling. Our hypothesis is that in such a system, more atmospheric information is introduced in near-native format to the orbit problem and it improves the solution accuracy.

5   Conclusions

265 Troposphere and stratosphere delay the propagation of navigation satellite signals and can lead to large errors in GNSS satellite orbit determination if not properly accounted for. In this article, a global numerical weather prediction model – OpenIFS of the European Centre for Medium-Range Weather Forecasts – is applied to generate atmospheric data of pressure, temperature, and humidity. These are converted to 3-dimensional atmospheric refraction fields and used as an input for ray-tracing to solve the least travel time signal paths from satellites to receiver stations and to compute the associated delays. These delays are

270 then directly used as *a priori* corrections of the atmospheric effects to solve GNSS satellite orbits with the GROOPS software toolkit of Graz University of Technology, Austria.

     This new configuration to solve the GNSS orbit problem contains two novel aspects. First, the direct use of tropospheric delays on slanted signal paths allows to fully account for the azimuthal asymmetries in the atmospheric refraction field, in contrast to traditional mapping functions which regularize the refraction field. Second, the intimate coupling of the numerical

275 weather prediction model with the orbit solver allows to control the information flow between the two modules, including output frequency of the weather model, for instance.

The main finding here is that the new configuration provides good consistency of GNSS satellite orbits as measured with the so-called orbit midnight discontinuities, i.e., how much satellite orbit initial positions need to be corrected between subsequent 24-hour orbit solutions. Another important finding is that the new configuration provides a solid reference where weather model-based data is directly interfaced with GNSS measurements and orbit solutions. Since the new configuration has fewer intermediate processing steps than the state-of-the-art methods, more direct diagnosis of the system performance is possible. In particular, this led us to detect a bias in our ray tracing computation that was undetected until now. Finally, the results indicate that azimuthal asymmetries in the tropospheric delays, which are well-preserved in the new configuration, contribute to the accuracy of orbit solutions. These asymmetries are not systematic but they have a systematic impact on the orbit solutions.

At a more general level, the new configuration provides an enhanced control of geodetic and meteorological aspects of the orbit problem. This will allow us to widely benefit the apparent synergies in space geodesy and meteorology.

Appendix A: The experiment using June 2017 data

The experimental results for the month of June 2017 are presented here. The experimental setup is identical to the experiment covering the month of December 2016. The central results, following the presentation of Section 2.4, are shown below.

(a) (b)
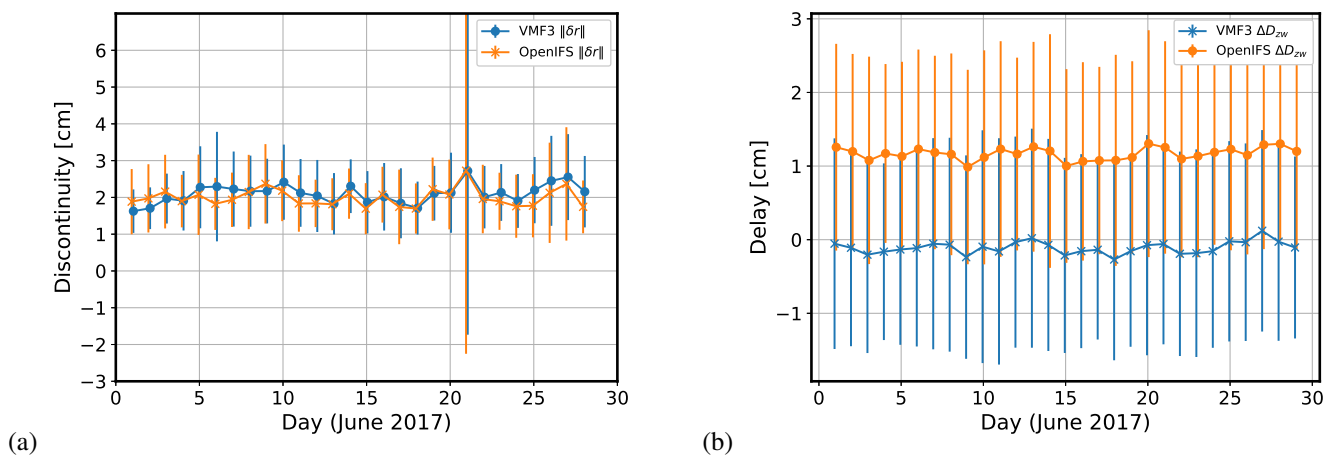
Figure A1. Daily means of (a) the midnight discontinuities and (b) the fitted zenith wet delays (ΔD_{zw}) of the default model (blue) and the experiment model (orange) for the month of June 2017.

Figure A1a can be compared to Fig. 1b, showing the daily mean of the midnight discontinuities of the *a priori* systems for the month. The overall means and standard deviations for the months of December 2016 and June 2017 are: (1.961 ± 0.903) cm and (1.996 ± 1.028) cm for the experimental system and (1.986 ± 0.907) cm and (2.102 ± 1.034) cm for the default system.

Figure A1b can be compared to Fig. 2a, showing the fitted parameters of the zenith wet delay (ΔD_{zw}). The bias in the experimental system for December 2016 (Fig. 2a) appears to be at a similar level also in June 2017. The overall mean and standard deviation in the experimental system is (1.220 ± 1.391) cm for December 2016 and (1.168 ± 1.371) cm for June

2017. On the other hand, the negligible bias (10^{-2} cm) in the default system in December 2016 seems to be slightly moved to negative for June 2017, although the overall standard deviation is very similar: (0.016 ± 1.349) cm for December 2016 and (-0.108 ± 1.370) cm for June 2017.

Code availability. The source code of GROOPS is openly available on GitHub (https://github.com/groops-devs/groops). Licence for using OpenIFS NWP model can be requested from ECMWF user support (openifs-support@ecmwf.int), and the model can be downloaded from the ECMWF FTP site (ftp.ecmwf.int). The LTT-operator used in this study is available on Zenodo under Creative Commons Attribution 4.0 International licence (https://doi.org/10.5281/zenodo.4834411; Eresmaa et al. 2021).

Data availability. Availability of the OpenIFS initial states is described in Ollinaho et al. (2021). GNSS observation data are kindly provided by the IGS via its data centers (https://igs.org/data-products-overview).

Author contributions. ANT performed experimentation and most of the data analysis, SS prepared and supervised the experimentation, LT ran the OpenIFS model and post-processed slant delay data, MV made the slant delay sensitivity analyses, maintained the LTT operator, and participated in production of the slant delay data, MP supported development of the concept, TMG provided in-depth expertise in the experimental design and supervised in all aspects of the project, and HJ supervised in all aspects of the project as its originator. All authors contributed to writing with coordination of HJ.

Competing interests. There are no competing interests.

Acknowledgements. We gratefully acknowledge support of the Doctoral Programme in Atmospheric Sciences in the University of Helsinki, and funding received from the Academy of Finland (grant number 1333034), the Vilho, Yrjö and Kalle Väisälä Foundation, and the Austrian Research Promotion Agency (FFG) under the Austrian Space Applications Programme (ASAP) Phase 16 (project number 878886). We would like to thank CSC - IT Center for Science in Finland - for their support in high-performance computing. Juha Lento from CSC is warmly acknowledged for his support and advice in implementing GROOPS in a massively parallel computing environment.

References

Arnold, D., Meindl, M., Beutler, G., Dach, R., Schaer, S., Lutz, S., Prange, L., Sośnica, K., Mervart, L., and Jäggi, A.: CODE's new solar radiation pressure model for GNSS orbit determination, Journal of Geodesy, 89, 775–791, https://doi.org/10.1007/s00190-015-0814-4, 2015.

320 Bauer, P., Thorpe, A., and Brunet, G.: The quiet revolution of numerical weather prediction, Nature, 525, 47–55, https://doi.org/10.1038/nature14956, 2015.

Bevis, M., Businger, S., Herring, T., Rocken, C., Anthes, R., and Ware, R.: GPS Meteorology: Remote Sensing of Atmospheric Water Vapour Using the Global Positioning System, Journal of Geophysical Research, 97, 15 787–15 801, https://doi.org/10.1029/92JD01517, 1992.

Böhm, J., Niell, A., Tregoning, P., and Schuh, H.: Global Mapping Function (GMF): A new empirical mapping function based on numerical
325 weather model data, Geophysical Research Letters, 33, https://doi.org/10.1029/2005GL025546, 2006.

Chen, G. and Herring, T. A.: Effects of atmospheric azimuthal asymmetry on the analysis of space geodetic data, Journal of Geophysical Research: Solid Earth, 102, 20 489–20 502, https://doi.org/10.1029/97JB01739, 1997.

CSC: CSC user guide, https://docs.csc.fi/computing/available-systems/, 2021.

ECMWF: Changes in ECMWF model, https://www.ecmwf.int/en/forecasts/documentation-and-support/changes-ecmwf-model, 2019.

330 Eresmaa, R., Järvinen, H., Niemelä, S., and Salonen, K.: Asymmetricity of ground-based GPS slant delay data, Atmospheric Chemistry and Physics, 7, 3143–3153, https://doi.org/doi:10.5194/acp-7-3143-2007, 2007.

Eresmaa, R., , Järvinen, H., Nordman, M., Poutanen, M., and Luntama, J.-P.: Parameterization of tropospheric delay correction for mobile GNSS positioning: a case study of a cold front passage, Meteorological Applications, 15, 447–454, https://doi.org/10.1002/met.86, 2008a.

Eresmaa, R., Healy, S., Järvinen, H., and Salonen, K.: Implementation of a ray-tracing operator for ground-based GPS Slant Delay observa-
335 tion modeling, Journal of Geophysical Research: Atmospheres, 113, https://doi.org/10.1029/2007JD009256, 2008b.

Eriksson, D., MacMillan, D., and Gipson, J.: Tropospheric delay ray tracing applied in VLBI analysis, Journal of Geophysical Research Solid Earth, 119, 9156–9170, https://doi.org/10.1002/2014JB011552., 2014.

Guerova, G., Jones, J., Douša, J., Dick, G., de Haan, S., Pottiaux, E., Bock, O., Pacione, R., Elgered, G., Vedel, H., and Bender, M.: Review of the state of the art and future prospects of the ground-based GNSS meteorology in Europe, Atmospheric Measurement Technique, 9,
340 5385–5406, https://doi.org/10.5194/amt-9-5385-2016, 2016.

Hauschild, A.: Basic Observation Equations, in: Springer Handbook of Global Navigation Satellite Systems, edited by Teunissen, P. J. and Montenbruck, O., Springer Handbooks, pp. 561–582, Springer International Publishing, Cham, https://doi.org/10.1007/978-3-319-42928-1_19, 2017.

Herring, T. A.: Modeling atmospheric delays in the analysis of space geodetic data, in: Proceedings of Refraction of Transatmospheric
345 Signals in Geodesy, edited by DeMunck, J. C. and Spoelstra, T. A. T., vol. 36 of *Netherlands Geodetic Commission Series*, pp. 57–164, The Hague, Netherlands, 1992.

Hobiger, T., Ichikawa, R., Takasu, T., Y, K., and Kondo, T.: Ray-traced troposphere slant delays for precise point positioning, Earth Planets and Space, 60, e1–e4, https://doi.org/doi.org/10.1186/BF03352809, 2008.

Hugentobler, U. and Montenbruck, O.: Satellite Orbits and Attitude, in: Springer Handbook of Global Navigation Satellite Sys-
350 tems, edited by Teunissen, P. J. and Montenbruck, O., Springer Handbooks, pp. 59–90, Springer International Publishing, Cham, https://doi.org/10.1007/978-3-319-42928-1_3, 2017.

Johnston, G., Riddell, A., and Hausler, G.: The International GNSS Service, in: Springer Handbook of Global Navigation Satellite Systems, edited by Teunissen, P. J. and Montenbruck, O., Springer Handbooks, pp. 967–982, Springer International Publishing, Cham, https://doi.org/10.1007/978-3-319-42928-1_33, 2017.

355 Landskron, D. and Böhm, J.: VMF3/GPT3:refined discrete and empirical troposphere mapping functions, Journal of Geodesy, 92, 349–360, https://doi.org/10.1007/s00190-017-1066-2, 2018.

Mayer-Gürr, T., Behzadpour, S., Eicker, A., Ellmer, M., Koch, B., Krauss, S., Pock, C., Rieser, D., Strasser, S., Suesser-Rechberger, B., Zehentner, N., and Kvas, A.: GROOPS: A software toolkit for gravity field recovery and GNSS processing, https://doi.org/10.1002/ESSOAR.10505041.1, 2020.

360 Niell, A.: Global mapping functions for the atmosphere delay at radio wavelengths, Journal of Geophysical Research, 101(B2), 3227–3246, 1996.

Nordman, M., Eresmaa, R., Poutanen, M., Järvinen, H., Koivula, H., and Luntama, J.-P.: Using numerical weather prediction model derived tropospheric slant delays in GPS processing: a case study, Geophysica, 43, 49–57, 2007.

Nordman, M., Eresmaa, R., Boehm, J., Poutanen, M., Koivula, H., and Järvinen, H.: Effect of troposphere slant delays on regional double

365 difference GPS processing, Earth Planets Space, 61, 845–852, 2009.

Ollinaho, P., Carver, G. D., Lang, S. T. K., Tuppi, L., Ekblom, M., and Järvinen, H.: Ensemble prediction using a new dataset of ECMWF initial states – OpenEnsemble 1.0, Geoscientific Model Development, 14, 2143–2160, https://doi.org/10.5194/gmd-14-2143-2021, 2021.

Petit, G. and Luzum, B., eds.: IERS Conventions (2010), IERS Technical Note 36, Verlag des Bundesamts für Kartographie und Geodäsie, Frankfurt am Main, https://www.iers.org/IERS/EN/Publications/TechnicalNotes/tn36.html, 2010.

370 Rocken, C., Sokolovskiy, S., Johnson, J. M., and Hunt, D.: Improved mapping of tropospheric delays, Journal of Atmospheric and Oceanic Technology, 18, 1205–1213, 2001.

Rodgers, C. D.: Inverse Methods for Atmospheric Sounding, Theory and Practice, 2, 256pp., https://doi.org/10.1142/3171, 2000.

Schönemann, E.: Analysis of GNSS raw observations in PPP solutions, Schriftenreihe der Fachrichtung Geodäsie, 42, https://tuprints.ulb.tu-darmstadt.de/3843/, 2014.

375 Schönemann, E., Becker, M., and Springer, T.: A new Approach for GNSS Analysis in a Multi-GNSS and Multi-Signal Environment, Journal of Geodetic Science, 1, 204–214, https://doi.org/10.2478/v10156-010-0023-2, 2011.

Strasser, S., Mayer-Gürr, T., and Zehentner, N.: Processing of GNSS constellations and ground station networks using the raw observation approach, Journal of Geodesy, 93, 1045–1057, https://doi.org/10.1007/s00190-018-1223-2, 2019.

Zus, F., Dick, G., Dousa, J., Heise, S., and Wickert, J.: The rapid and precise computation of GPS slant total delays and mapping factors

380 utilizing a numerical weather model, Radio Science, 49, 207–216, https://doi.org/10.1002/2013RS005280, 2014.